

UC Irvine

UC Irvine Previously Published Works

Title

Crystal structure and functional analysis of Leishmania major pseudoperoxidase

Permalink

<https://escholarship.org/uc/item/9sf197wv>

Journal

JBIC Journal of Biological Inorganic Chemistry, 22(6)

ISSN

0949-8257

Authors

Chreifi, Georges
Dejam, Dillon
Poulos, Thomas L

Publication Date

2017-08-01

DOI

10.1007/s00775-017-1469-9

Peer reviewed



Published in final edited form as:

J Biol Inorg Chem. 2017 August ; 22(6): 919–927. doi:10.1007/s00775-017-1469-9.

Crystal Structure and Functional Analysis of *Leishmania major* Pseudoperoxidase

Georges Chreifi^{1,#}, Dillon Dejam^{1,#}, and Thomas L. Poulos^{1,2,3,*}

¹Department of Molecular Biology and Biochemistry, University of California, Irvine, California 92697-3900

²Department of Chemistry, University of California, Irvine, California 92697-3900

³Department of Pharmaceutical Sciences, University of California, Irvine, California 92697-3900

Abstract

Leishmania major pseudoperoxidase (LmPP) is a recently discovered heme protein expressed by the human pathogen. Previous *in vivo* and *in vitro* studies suggest that LmPP is a crucial element of the pathogen's defense mechanism against the reactive nitrogen species peroxynitrite produced during the host immune response. In order to shed light on the potential mechanism of peroxynitrite detoxification, we have determined the 1.76-Å X-ray crystal structure of LmPP, revealing a striking degree of homology with heme peroxidases. The most outstanding structural feature is a Cys/His heme coordination, which corroborates previous spectroscopic and mutagenesis studies. We also used a combination of stopped-flow and electron paramagnetic spectroscopies that together suggest that peroxynitrite is not a substrate for LmPP catalysis, leaving the function of LmPP an open question.

Keywords

heme; x-ray crystallography; peroxynitrite; stopped-flow spectroscopy; peroxidase; *Leishmania*

Introduction

The *Leishmania* parasite causes cutaneous and visceral leishmaniasis, the latter disease resulting in severe internal symptoms and in nearly 100% fatality when left untreated [1]. While treatment is available, current treatments exhibit sub-optimal efficiency [2]. An increased understanding of *Leishmania* spp. associated pathology would be helpful to better diagnose and treat cases of leishmaniasis. Upon infection, *L. major* is rapidly phagocytized by host macrophages and is able to survive exposure to large quantities of reactive oxygen and nitrogen intermediates derived from hydrogen peroxide (H₂O₂), superoxide (O₂⁻), and nitric oxide (NO) [3]. While the enzymatic mechanisms involved in detoxifying H₂O₂ and O₂⁻ are well established [4–7], those by which the *Leishmania* parasite protects itself from

*Corresponding author: poulos@uci.edu; 949-824-7020.

#G.C. and D.D. are co-first authors.

†Coordinates and structure factors have been deposited in the Protein Data Base under accession number 5VIA.

NO or ONOO⁻ (peroxynitrite, PN) are poorly understood. PN is the product of the irreversible reaction between NO and O₂⁻ radicals, with a rate constant of up to ~10¹⁰ M⁻¹ s⁻¹ [8] and a ΔG of -22 kcal · mol⁻¹ [9]. Acting as both a 2-electron oxidant and a strong nucleophile, PN is highly deleterious *in vivo* and has been shown to hydroxylate cysteine sulfhydryls [10–12], nitrate tyrosine side-chains [13–14], and both oxidize and nitrate transition metal centers [15–16]. PN has also been shown to possess leishmanicidal activity both *in vivo* and *in vitro* [17].

Recently, a novel heme enzyme in *L. major* has been identified and hypothesized to be a PN scavenger [18], providing a novel therapeutic target to increase susceptibility of the pathogen to reactive nitrogen species. Because of its high sequence similarity (14% identical, 40% conserved) to the well-studied *L. major* heme peroxidase (LmP), but inability to use H₂O₂ as a substrate, it was dubbed *L. major* pseudoperoxidase (LmPP). Localization of the protein was determined by immunofluorescence microscopy, revealing an eight-fold increase in expression in the non-flagellar amastigote form compared to the flagellar promastigote form, as well as localization to the plasma membrane [18]. Gene knockout studies indicate that LmPP is necessary for both disease development in mice, as well as resistance to nitrogen-mediated killing in macrophages [18]. Additionally, rapid kinetic experiments revealed a 4-fold increase in PN decay in the presence of LmPP [18]. UV/Vis spectroscopic studies also showed that the addition of PN causes a shift in the LmPP heme iron from ferric 6-coordinate low spin state to ferric high spin state in the absence of an electron donor. While mutagenesis studies point to His²⁰⁶ and Cys¹⁰⁷ as the likely proximal and distal axial heme ligands, respectively [19], the absence of a crystal structure has been an obstacle to determining the mechanism of PN detoxification by LmPP. Here, we describe the 1.76-Å crystal structure of LmPP, in addition to kinetic and spectroscopic studies, in order to shed further light on the potential biological function of this intriguing heme protein.

Methods

Molecular Cloning

The wild type LmPP gene without the hydrophobic N-terminal tail, as 48LmPP, was obtained from Dr. Subrata Adak. 48LmPP was first cloned into the pET28a vector with kanamycin resistance and an N-terminal 6X-Histidine tag, between the NdeI and XhoI restriction sites. First, a polymerase chain reaction (PCR) was used to amplify the 48LmPP gene. An empty pET28a vector and the amplified PCR product were both digested with restriction enzymes NdeI and XhoI in order to produce compatible ends for ligation. The digested gene fragment was then ligated into the vector using T4 DNA ligase to generate the pET28a/ 48LmPP plasmid. Successful cloning was confirmed by agarose gel electrophoresis and DNA sequencing.

Expression and Purification of Wild Type LmPP

The pET28a/ 48LmPP plasmid was transformed into *E. coli* BL21(DE3) cells and cultured in 2xYT medium for 8 hours before inoculation into TB medium (50 µg/mL kanamycin). Expression cultures were grown at 37 °C, 270 RPM for approximately 18 hours before induction with 0.5 mM isopropyl β-D-1-thiogalactopyranoside and 0.4 mM δ-

aminolevulinic acid, a heme precursor. Cultures were then allowed to persist at room temperature, 100 RPM for 24 hours before they were harvested by centrifugation.

Cells were resuspended in Buffer A (50 mM potassium phosphate pH 7.8, 100 mM potassium chloride, and 5 mM β -mercaptoethanol). Resuspended cells were lysed using a microfluidizer at 18,000 psi (Microfluidics International Co) in buffer A containing an additional 1 mM phenylmethanesulfonyl fluoride (PMSF). The resulting suspension was centrifuged at 17,000 rpm in order to separate insoluble cell debris. Supernatant cell-free extract from centrifugation was then loaded onto a Ni²⁺-Nitrilotriacetate (Ni-NTA) column previously equilibrated with 10 column volumes (CV) of buffer A. The column was then washed with 10 CV of Buffer A and 10 CV of Buffer A with 5 mM L-histidine (L-His) in order to wash away loosely bound contaminants and eluted with a linear gradient of 5 to 100 mM L-His in buffer A. Wild-type LmPP was previously reported to display an absorbance peak at 423 nm with a molar extinction coefficient of 65 mM⁻¹ cm⁻¹. [18] The R_Z ratio (OD₄₂₃/OD₂₈₀) was used as a metric to assess the purity of each fraction, and fractions with R_Z greater than 1.2 were pooled.

The pooled fractions were then digested by thrombinolysis in order to cleave the polyhistidine-tag using a 50:1 weight ratio of LmPP and a 2 hour incubation at 25 °C. The reaction was quenched with PMSF and loaded onto a fresh Ni-NTA column previously equilibrated with 10 CV of buffer A. Buffer A containing 5 mM L-His was used for elution and colored fractions were pooled and dialyzed overnight against Buffer B (12.5 mM potassium phosphate pH 5.3, 12.5 mM potassium chloride, and 0.5 mM dithiothreitol (DTT)) and loaded onto a high performance SP sepharose cation exchange column. The column was preequilibrated with Buffer C (50 mM potassium phosphate pH 5.3, 50 mM potassium chloride, and 2 mM DTT). Protein was eluted with a fractionated gradient of 50–550 mM potassium chloride in buffer C, and the resulting fractions with R_Z values greater than 1.4 were pooled.

The protein was then loaded onto a 16/60 Superdex 75 gel filtration column preequilibrated with Buffer D (50 mM potassium phosphate pH 7.0, 5% v/v glycerol and 2 mM DTT), and fractions with R_Z values greater than 1.4 were combined. Protein purity was confirmed by SDS-page.

LmPP Crystallization, Structure Determination, and Refinement

Hanging drop vapor diffusion crystals were set up with 14 mg/mL LmPP in a well solution containing 5% 2-methyl-2,4-pentanediol, 10% polyethylene glycol 6000, and 0.1 M HEPES pH 7.5. Crystals were harvested, soaked step-wise in a cryoprotectant solution containing 30 % glycerol, and flash frozen in liquid nitrogen. Cryogenic (100 K) X-ray diffraction data were collected remotely at the Stanford Synchrotron Radiation Lightsource (SSRL) facility, beamline 14-1, using the data collection control software Blu-Ice [20]. Crystals were first screened for diffraction quality by taking two snapshots (90° rotation, 1° width) with short X-ray exposure (5 s). The best diffracting crystal was chosen to collect multi-wavelength anomalous dispersion (MAD) data using the inverse beam protocol. A fluorescence scan was performed in order to determine the optimal wavelengths for anomalous dispersion near the Fe absorption edge. Two full datasets were collected at different wavelengths ($\lambda_{\text{inflection}} =$

1.74 Å and $\lambda_{\text{remote}} = 1.65$ Å). Another crystal was used to obtain a high resolution dataset at the maximum energy of beamline 14-1 ($\lambda_{\text{highres}} = 1.18$ Å). iMOSFLM [21] was used to index and integrate the reflections, and POINTLESS and AIMLESS were used to scale and merge the data. PHENIX AutoSol [22] was used to simultaneously process the data, determine phase values and calculate an initial electron density map. PHENIX AutoBuild [23] was then used to build an initial model into the electron density, and phenix.refine [24] to refine this model against the high resolution data set. Refinement was performed until R_{work} and R_{free} reached suitable values, and COOT [25] was used to build and validate the finished model.

Electron Paramagnetic Resonance Spectroscopy

LmPP resting state EPR samples were prepared with 0.1 mM LmPP in 0.1 M Tris, pH 9. Timecourse reaction samples were prepared by first mixing 0.1 mM LmPP with 10 mM peroxyntirite in 0.1 M Tris pH 9.0, transferred to an EPR tube, and flash frozen in liquid N₂ 10 s, 30 s, and 60 s after the reaction was initiated. Cryogenic (10 K) X-band (9.64 GHz) EPR spectra were recorded on a Bruker EMX EPR spectrometer equipped with an Oxford ESR 900 liquid helium cryostat. The modulation frequency and amplitude was 100 kHz and 10.02 G. The EPR simulation software package SpinCount [26] was used to analyze the data.

Stopped-Flow Spectroscopy

All stopped-flow kinetic measurements were performed using an SX.20MV stopped-flow spectrophotometer (Applied Photophysics) with an instrument dead time of ~1.0 ms. Prepared LmPP and peroxyntirite solutions were loaded into separate 2.5 mL syringes and injected into two separate drive syringes of the stopped-flow instrument. LmPP solutions were prepared in either 0.1 M potassium acetate pH 4.4, 0.1 M potassium phosphate pH 6.0, 6.5, or 7.0, or 0.1M Tris pH 9. Peroxyntirite solutions were prepared in 0.5 mM NaOH where >95% remained stable after an hour. In sequential mixing experiments, peroxyntirite solution was mixed with buffer and aged for a certain period before mixing with LmPP solution. Single wavelength absorptions were measured at various wavelengths (423 nm = resting state LmPP, 302 nm = peroxyntirite) using a photomultiplier detector, while a photodiode array detector was used to collect full spectrum scans. Rate constants were calculated using the software provided with the stopped-flow instrument (Applied Photophysics) and the following standard single exponential equation:

$$A_{302} = C_1 e^{-k_{\text{obs}} t} + b$$

where C is the amplitude term, k_{obs} is the observed rate constant for the decay of peroxyntirite at 302 nm, and b is an off-set value.

Results & Discussion

LmPP Purification and Crystal Structure

LmPP was purified to $R_Z(A_{423}/A_{280}) = 1.4$ (Figure S1), higher than previously reported R_Z of 1.2 [18] and the resulting protein solution was red-orange in color. Crystals formed overnight, and there was no visible precipitate in the drops. After multiple rounds of refinement, the crystal structure of LmPP was solved to 1.76-Å using multi-wavelength anomalous dispersion (MAD) and submitted to the Protein Data Bank (PDB ID 5VIA). Crystallographic data and refinement statistics are recorded in Table 1.

The overall three-dimensional fold of LmPP shows remarkable similarity with the fold of other peroxidases (Figure 1A). Non-mammalian peroxidases are divided into three classes: class I are intercellular peroxidases, class II are extracellular fungal peroxidases, and class III are extracellular plant peroxidases [27]. Peroxidases of all 3 classes, including *L. major*'s class I peroxidase LmP, have a single His-coordinated to the heme iron, and are composed of 10 α -helices and a single antiparallel β -sheet consisting of 3 beta strands, whereas LmPP contains 11 α -helices and a single antiparallel β -sheet consisting of 2 beta strands. Compared to LmP, LmPP also possesses an additional loop on the distal side of the heme that contains Cys¹⁰⁷, the heme distal axial ligand. In order to quantify the differences, we calculated the root-mean-square deviations (rmsds) of the LmP polypeptide chain (PDB entry 3RIV) superposed with the LmPP chain (Figure 1B), which gave an rmsd value of 1.04 Å for 143 matching residues, and an rmsd value of 4.27 Å for the total structures when including mismatched surface loops.

Our crystal structure confirms previous work identifying the LmPP axial ligands using a combination of site-directed mutagenesis and UV/Vis spectrophotometry [19]. The heme is coordinated proximally by His²⁰⁶ and distally by Cys¹⁰⁷ (Figure 2A). This type of His/Cys ligation is relatively uncommon among heme proteins. To date, there are no known His/Cys ligated heme proteins with catalytic capabilities that involve the heme group. Cystathionine- β synthase also has a His/Cys ligated heme b protein, but the catalytic activity of this enzyme is preserved even after heme displacement, suggesting a regulatory role modulated by redox changes [28]. Certain heme sensor proteins also have His/Cys ligation [29] where the Cys is readily dissociated, but here too, there is no catalytic activity associated with the heme group.

The structure shows a solvent-access channel located on the distal side of the heme and analogous to the one found in LmP, suggesting that a potential substrate would interact on the distal side of the heme, although dissociation of Cys¹⁰⁷ would be required in order to access the iron. On the proximal side, the axial ligand His²⁰⁶ forms π -stacking interactions with a neighboring residue, His223. In other peroxidases, such as ascorbate peroxidase (APX), cytochrome c peroxidase (CcP), and LmP, the analogous residue is a tryptophan (Figure 2B). In LmP and CcP, this tryptophan forms a π -cationic radical that stabilizes the formation of the first reactive intermediate, Compound I ($\text{Fe}^{\text{IV}}=\text{O})\text{Trp}^+$, which is a characteristic intermediate in heme enzyme catalysis [30–31]. However, in other peroxidases, such as APX, the radical is located on the porphyrin ring [32]. The substitution

of Trp by His at this position suggests that if LmPP has a similar catalytic cycle to peroxidases, then the π -cationic radical most likely would form on the porphyrin.

Another feature on the proximal side of the heme is the presence of Glu²¹⁹. In CcP and LmP, the analogous residue is an Asp that forms a hydrogen bond with the proximal His ligand and confers a partial imidazolate character. The length of the Asp²⁵³-His¹⁹² hydrogen bond in LmP is 2.90 Å (Figure 2B), 2.92 Å for the Asp²³⁵-His¹⁷⁵ H-bond in CcP (Figure 2C), while the length of the Glu²¹⁹-His²⁰⁶ hydrogen bond in LmPP is 2.56 Å (Figure 2A), suggesting that the proximal His ligand of LmPP may have a relatively greater imidazolate character than that of LmP and CcP.

Many peroxidases possess an Arg residue on the distal side of the heme. Arg³⁸ in APX has been shown to be crucial for the formation of the heme ferryl species [33] and Arg³⁸ in horse radish peroxidase (HRP) has been shown to be involved in the cleavage of the peroxide O-O bond, as well as in the binding of peroxide to HRP [34]. LmPP also has an Arg at this position, yet reactivity with peroxide is still extremely low [18], which in part has been attributed to the fact that LmPP has a distal Val⁹⁰ that replaces the distal catalytic His found in peroxidases. The distal His has been shown to be crucial to the formation of Compound I in many peroxidases [35–36] as well as in the reduction of Compound II [37]. Studies on Val⁹⁰ to His LmPP mutants have shown that H₂O₂ turnover and peroxidase-like activity is restored [38]. However, the distal Cys¹⁰⁷ must first be artificially dissociated through an unknown mechanism by mixing 5 μ M LmPP with both 5 μ M H₂O₂ and 10 μ M 2,2'-azino-bis(3-ethylbenzothiazoline-6-sulphonic acid) (ABTS) in 50 mM phosphate, pH 5.5. We have attempted to react LmPP with H₂O₂ alone, and with both H₂O₂ and ABTS simultaneously, both of which resulted in no discernible shift in the UV/Vis spectrum (data not shown).

Stopped-Flow Spectroscopy

We used stopped-flow spectroscopy to probe the interactions and mechanism of PN detoxification by LmPP and trap any spectroscopically visible intermediate in the reaction. Concentrations lower than 100-fold excess peroxyxynitrite did not result in an observable Soret peak shift, nor in a change in PN decay rate, but does result in some heme decay (Figure 3), and suggests that no catalysis occurs, but only heme degradation. Since the pK_a of ONOOH is 6.8 [10], we initially attributed the lack of a reaction to the instability of PN at neutral and acidic pH and, therefore, characterized this reaction at a broader pH range. PN is significantly more stable at higher pH, with a measured decay rate constant of 1.39 min⁻¹ at pH 9 compared to 13.0 min⁻¹ at pH 7.5 and 88.1 min⁻¹ at pH 4.4 (Table 2). At pH 9 with 100 fold excess PN, we do observe a shift from 423 nm to 408 nm (Figure S2D), which is consistent with dissociation of the Cys ligand and a His-ligated high spin heme. This is followed by heme degradation (Figure S2). The rate of heme decay also increases as a function of PN concentration, suggesting that either PN or a byproduct of PN decay is directly responsible for the observed heme destruction.

While the overall behavior observed was the same at all pH values (Figure S2), our results show that a greater concentration of PN is required to obtain similar shifts at acidic pH, suggesting that either ONOO⁻ is the reacting species, or that the poor reactivity is due to the

greater decay rate of ONOOH, which is the lesser stable species [39]. To ensure that destruction of the heme was not masking a true shift, we performed the reaction at 4 °C, which resulted in a 3-fold reduction in PN decay rate (Table 2), but no isolated peak shift was observed while the heme absorption peak decayed over more than 16 min. (Figure S3). Overall, the behavior observed when LmPP is exposed to large concentrations of PN suggests that PN causes dissociation and possible modification of one of the heme ligands, most likely Cys¹⁰⁷, and that either the remaining PN itself, or reactive byproducts of PN decay, assault the heme metal center, resulting in heme destruction.

To test if PN byproducts react with LmPP, we performed sequential stopped-flow mixing in order to probe interactions between LmPP and PN byproducts by allowing PN to decay for a known delay time before being mixed with LmPP. As expected, we observed a decrease in percentage of PN introduced into the reaction mixture as delay time is increased, from 43% remaining after 0.1s delay time, to 5.8% remaining after 10s delay time. Our sequential stopped-flow results (Figure S4) also show that the rate of Soret shift from low spin to high spin, as well as the rate of heme decay, decreases as the delay time increases, indicating that PN itself is in fact the species catalyzing the dissociation of the heme axial ligand, and not a PN byproduct.

Finally, we found no correlation between LmPP concentration and PN decay rate. With or without LmPP, the decay rate is about 27.0 min⁻¹ (Figure 4A). This rate is to be compared with 840 min⁻¹ for the reaction between PN and metmyoglobin (Mb) distal His mutants [40]. Since the crystal structure of LmPP shows a distal Val⁹⁰ instead of His, the metmyoglobin mutants can serve as a comparison of expected PN catalytic rate. Although previous studies using 30 μM LmPP resulted in a 4-fold increase in the decay of 800 μM PN [18], we were not able to obtain similar data. In fact, the rates we measured are not indicative of any catalytic involvement by LmPP, and in combination with our other data, suggest that PN consumption by LmPP occurs through mechanisms involving heme destruction rather than catalysis.

Electron Paramagnetic Resonance Spectroscopy

The resting state EPR spectrum of LmPP exhibits a single spin 1/2 signal ($g_x = 2.53$, $g_y = 2.25$, $g_z = 1.78$) at 10 K (Figure 5A and B), consistent with a 6-coordinate low spin heme and with previously reported values [18]. In order to capture the intermediates of the reaction between PN and LmPP, we added 100-fold excess PN in 0.1M Tris, pH 9.0, quenched the reactions by flash-freezing into liquid nitrogen after 10s, 30s, and 60s, and measured their respective X-band EPR spectra at 10 K (Figure 5C and D). These spectra reveal a spin 5/2 signal ($g_{\perp} = 6.06$) that appears and increases in intensity over time, while the spin 1/2 signal observed in the resting state EPR simultaneously decreases in intensity, suggesting that the 6-coordinate low spin heme is converting to 5-coordinate high spin heme. Some spin 1/2 signal is still observed, indicating that not all of the heme is converted during the 60s time course of the reaction. We also observe a very sharp spin 1/2 signal (approximately 50 Gauss thickness) with $g = 2.00$ and of much larger magnitude, typical of organic radicals, along with the appearance of a large signal at $g = 4.27$, suggesting the presence of adventitious Fe^{III}, both of which also increase in intensity over the course of the

reaction. Taken together, these data suggest that the addition of 100-fold excess of peroxyxynitrite has 3 direct effects: i) dissociation of one of the heme ligands, most likely Cys¹⁰⁷, generating high spin heme; ii) oxidation of a number of LmPP residues into their corresponding organic radical species, resulting in protein destruction; and iii) heme destruction and subsequent release of adventitious Fe^{III}. These observations correlate well with data observed by stopped-flow spectroscopy: shift to high spin followed by extensive heme degradation.

Conclusions

Our crystal structure reveals that LmPP shares a high degree of structural and topological homology with heme peroxidases, even though it lacks the ability to turnover H₂O₂. While the function of LmPP was initially proposed to bind and detoxify PN as a substrate, our results indicate that PN produces no detectable shift in the Soret peak at less than 100-fold excess PN, but does result in heme degradation. Reactions with concentrations of PN greater than 100-fold excess result in a shift to 5-coordinate high spin heme, followed by extensive decay of the heme absorption peak. Our stopped-flow and EPR data show that this shift and decay is caused by heme degradation and protein oxidation. His/Cys ligation is well known in various sensor proteins [29], but His/Cys ligation where the Cys ligand is not readily replaced has been observed only rarely. In none of the known examples does the His/Cys ligated heme participate directly in catalysis. For this to occur, one of the ligands, Cys in the case of LmPP, must dissociate in order to free the distal coordination site to interact with potential substrates. This appears to occur in our experiments, but only under extreme and certainly not physiological conditions. LmPP thus is very unlikely to serve as an enzyme for the elimination of PN. Nevertheless, previous *in vivo* experiments do suggest a role of LmPP in the protection against NO or its metabolites, since a LmPP knockout is much more susceptible to NO donors [18]. LmPP also is tethered to the plasma membrane by an N-terminal anchor that would enable LmPP to encounter host generated NO or other reactive oxygen species. Indeed, Cys/His ligated heme systems have presented a conundrum in the metalloprotein community. A close homolog to LmPP with respect to heme ligation is cystathionine- β -synthase (CBS), but unlike LmPP, CBS has been extensively studied and yet the function of the heme remains unknown. However, like CBS [41], the heme iron in LmPP can be reduced with dithionite, enabling formation of the ferrous-carbon monoxide (CO) complex. The spectral features of the CO complex are characteristic of His-ligation (Figure S6). Therefore, if there is a physiological reductant capable of reducing LmPP and displacing the Cys ligand, there could potentially be an enzymatic function for LmPP. However, like CBS, the ferric protein is inert.

Supplementary Material

Refer to Web version on PubMed Central for supplementary material.

Acknowledgments

This work was supported by NIH grant GM57353 (TLP). We thank Prof. Andrew S. Borovik, as well as Samuel Mann and Victoria Oswald for assistance with the EPR spectrometry, data collection, and analysis. We would also like to thank Dr. Huiying Li for help with the X-ray data collection, and Sarvind M. Tripathi for helpful discussions

in the early stages of this research, as well as the beamline staff at the Stanford Synchrotron Radiation Lightsource (SSRL) for their assistance during X-ray diffraction data collection.

References

1. Lukeš J, Mauricio IL, Schönian G, Dujardin J-C, Soteriadou K, Dedet J-P, Kuhls K, Tintaya KWQ, Jirk M, Chocholová E. *Proceedings of the National Academy of Sciences*. 2007; 104:9375–9380.
2. Chappuis F, Sundar S, Hailu A, Ghalib H, Rijal S, Peeling RW, Alvar J, Boelaert M. *Nature reviews microbiology*. 2007; 5:873–882. [PubMed: 17938629]
3. Murray M, Morrison W, Whitelaw D. *Advances in parasitology*. 1982; 21:1–68. [PubMed: 6762064]
4. Murray H. *Journal of Immunology*. 1982; 129:351–357.
5. Barr SD, Gedamu L. *Journal of Biological Chemistry*. 2001; 276:34279–34287. [PubMed: 11438539]
6. Lin Y-C, Hsu J-Y, Chiang S-C, Lee ST. *Molecular and biochemical parasitology*. 2005; 142:66–75. [PubMed: 15907561]
7. Ghosh S, Goswami S, Adhya S. *Biochemical Journal*. 2003; 369:447–452. [PubMed: 12459037]
8. Ferrer-Sueta G, Radi R. *ACS chemical biology*. 2009; 4:161–177. [PubMed: 19267456]
9. Huie RE, Padmaja S. *Free radical research communications*. 1993; 18:195–199. [PubMed: 8396550]
10. Beckman J, Koppenol W, Moreno J, Pryor W, Ischiropoulos H. *Chem Res Toxicol*. 1992; 5:834–842. [PubMed: 1336991]
11. Radi R, Beckman JS, Bush KM, Freeman BA. *Journal of Biological Chemistry*. 1991; 266:4244–4250. [PubMed: 1847917]
12. Quijano C, ALVAREZ B, GATTI RM, AUGUSTO O, Rafael R. *Biochemical Journal*. 1997; 322:167–173. [PubMed: 9078258]
13. Ischiropoulos H, Zhu L, Chen J, Tsai M, Martin JC, Smith CD, Beckman JS. *Archives of biochemistry and biophysics*. 1992; 298:431–437. [PubMed: 1416974]
14. Beckmann JS, Ye YZ, Anderson PG, Chen J, Accavitti MA, Tarpey MM, White CR. *Biological chemistry Hoppe-Seyler*. 1994; 375:81–88. [PubMed: 8192861]
15. Crow JP, Beckman JS, McCord JM. *Biochemistry*. 1995; 34:3544–3552. [PubMed: 7893650]
16. Hausladen A, Fridovich I. *Journal of Biological Chemistry*. 1994; 269:29405–29408. [PubMed: 7961919]
17. Linares E, Giorgio S, Mortara RA, Santos CX, Yamada AT, Augusto O. *Free Radical Biology and Medicine*. 2001; 30:1234–1242. [PubMed: 11368921]
18. Bose M, Saha R, Santara SS, Mukherjee S, Roy J, Adak S. *Free Radical Biology and Medicine*. 2012; 53:1819–1828. [PubMed: 22985938]
19. Saha R, Bose M, Sen Santara S, Roy J, Adak S. *Biochemistry*. 2013; 52:8878–8887. [PubMed: 24261670]
20. McPhillips TM, McPhillips SE, Chiu H-J, Cohen AE, Deacon AM, Ellis PJ, Garman E, Gonzalez A, Sauter NK, Phizackerley RP. *Journal of synchrotron radiation*. 2002; 9:401–406. [PubMed: 12409628]
21. Battye TGG, Kontogiannis L, Johnson O, Powell HR, Leslie AG. *Acta Crystallographica Section D: Biological Crystallography*. 2011; 67:271–281. [PubMed: 21460445]
22. Terwilliger TC, Adams PD, Read RJ, McCoy AJ, Moriarty NW, Grosse-Kunstleve RW, Afonine PV, Zwart PH, Hung L-W. *Acta Crystallographica Section D: Biological Crystallography*. 2009; 65:582–601. [PubMed: 19465773]
23. Terwilliger TC, Grosse-Kunstleve RW, Afonine PV, Moriarty NW, Zwart PH, Hung L-W, Read RJ, Adams PD. *Acta Crystallographica Section D: Biological Crystallography*. 2008; 64:61–69. [PubMed: 18094468]
24. Adams PD, Mustyakimov M, Afonine PV, Langan P. *Acta Crystallographica Section D: Biological Crystallography*. 2009; 65:567–573. [PubMed: 19465771]
25. Emsley P, Cowtan K. *Acta Crystallographica Section D: Biological Crystallography*. 2004; 60:2126–2132. [PubMed: 15572765]

26. Golombek AP, Hendrich MP. *Journal of Magnetic Resonance*. 2003; 165:33–48. [PubMed: 14568515]
27. Welinder KG. *Current Opinion in Structural Biology*. 1992; 2:388–393.
28. Meier M, Janosik M, Kery V, Kraus JP, Burkhard P. *The EMBO Journal*. 2001; 20:3910–3916. [PubMed: 11483494]
29. Shimizu T, Huang D, Yan F, Stranova M, Bartosova M, Fojtikova V, Martinkova M. *Chem Rev*. 2015; 115:6491–6533. [PubMed: 26021768]
30. Sivaraja M, Goodin DB, Smith M, Hoffman BM. *Science*. 1989; 245:738. [PubMed: 2549632]
31. Jasion VS, Polanco JA, Meharena YT, Li H, Poulos TL. *Journal of Biological Chemistry*. 2011; 286:24608–24615. [PubMed: 21566139]
32. Patterson WR, Poulos TL, Goodin DB. *Biochemistry*. 1995; 34:4342–4345. [PubMed: 7703248]
33. Efimov I, Badyal SK, Metcalfe CL, Macdonald I, Gumiero A, Raven EL, Moody PC. *Journal of the American Chemical Society*. 2011; 133:15376–15383. [PubMed: 21819069]
34. Rodriguez-Lopez JN, Smith AT, Thorneley RN. *Journal of Biological Chemistry*. 1996; 271:4023–4030. [PubMed: 8626735]
35. Erman JE, Vitello LB, Miller MA, Shaw A, Brown KA, Kraut J. *Biochemistry*. 1993; 32:9798–9806. [PubMed: 8396972]
36. Newmyer SL, deMontellano PRO. *Journal of Biological Chemistry*. 1995; 270:19430–19438. [PubMed: 7642625]
37. Chreifi G, Baxter EL, Doukov T, Cohen AE, McPhillips SE, Song J, Meharena YT, Soltis SM, Poulos TL. *Proceedings of the National Academy of Sciences*. 2016; 113:1226–1231.
38. Saha R, Bose M, Adak S. *Biochimica et Biophysica Acta (BBA)-Proteins and Proteomics*. 2013; 1834:651–657. [PubMed: 23277197]
39. Tsai J-HM, Harrison JG, Martin JC, Hamilton TP, van der Woerd M, Jablonsky MJ, Beckman JS. *Journal of the American Chemical Society*. 1994; 116:4115–4116.
40. Herold S, Matsui T, Watanabe Y. *Journal of the American Chemical Society*. 2001; 123:4085–4086. [PubMed: 11457162]
41. Carballal S, Cuevasanta E, Yadav PK, Gherasim C, Ballou DP, Alvarez B, Banerjee R. *J Biol Chem*. 2016; 291:8004–8013. [PubMed: 26867575]
42. Pettersen EF, Goddard TD, Huang CC, Couch GS, Greenblatt DM, Meng EC, Ferrin TE. *Journal of computational chemistry*. 2004; 25:1605–1612. [PubMed: 15264254]

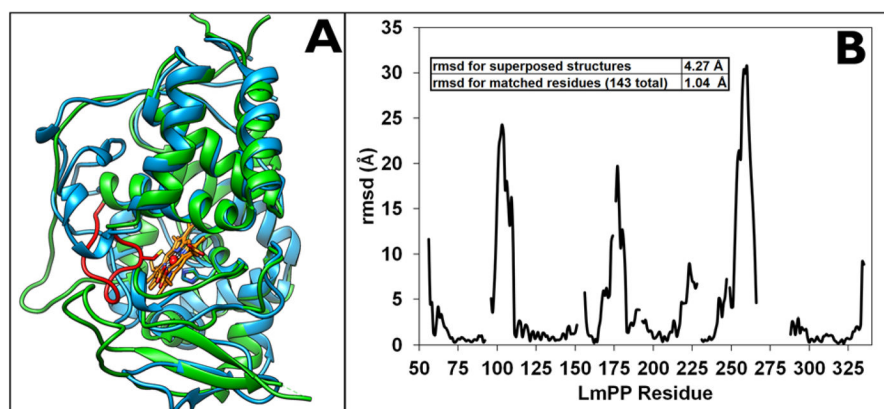


Figure 1. (A) α -carbon backbone superposition of LmPP and LmP (PDB entry 3RIV) shows the striking degree of structural similarity between the two enzymes. LmP is depicted in cyan, LmPP in green, and the LmPP loop that contains Cys¹⁰⁷ and is not present on LmP is depicted in red. All molecular graphic images were generated using UCSF Chimera [42]. (B) root-mean-square deviations (rmsds) for the superposition of chain A of LmPP with Chain A of LmP (PDB entry 3RIV), done with UCSF chimera Matchmaker, using the Needleman-Wunsch alignment algorithm and BLOSUM-62 matrix [42].

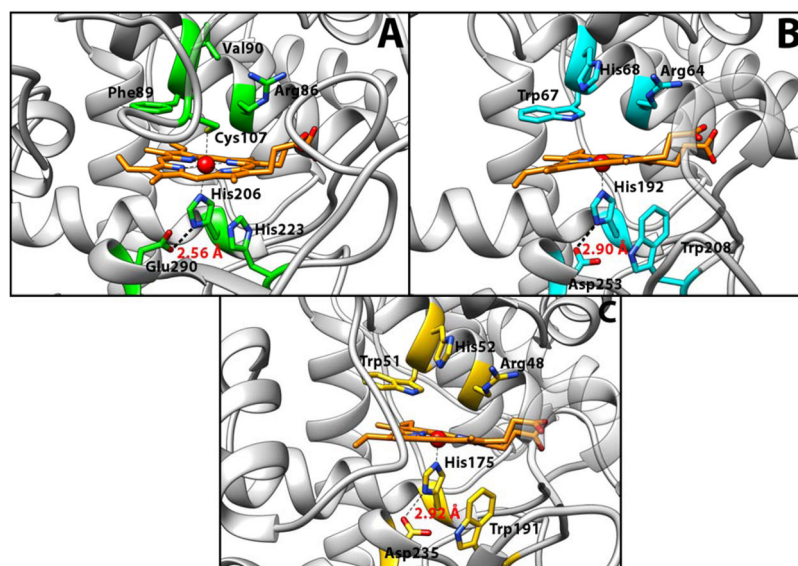


Figure 2.
(A) Architecture of the active site of wild type LmPP. Residues in the active site pocket are depicted in green (B) Architecture of the active site of wild type LmP (PDB entry 3RIV). For contrast, residues in the active site pocket are depicted in cyan. (C) Architecture of the active site of wild type CcP (PDB entry 2CYP), with analogous active site residues depicted in yellow.

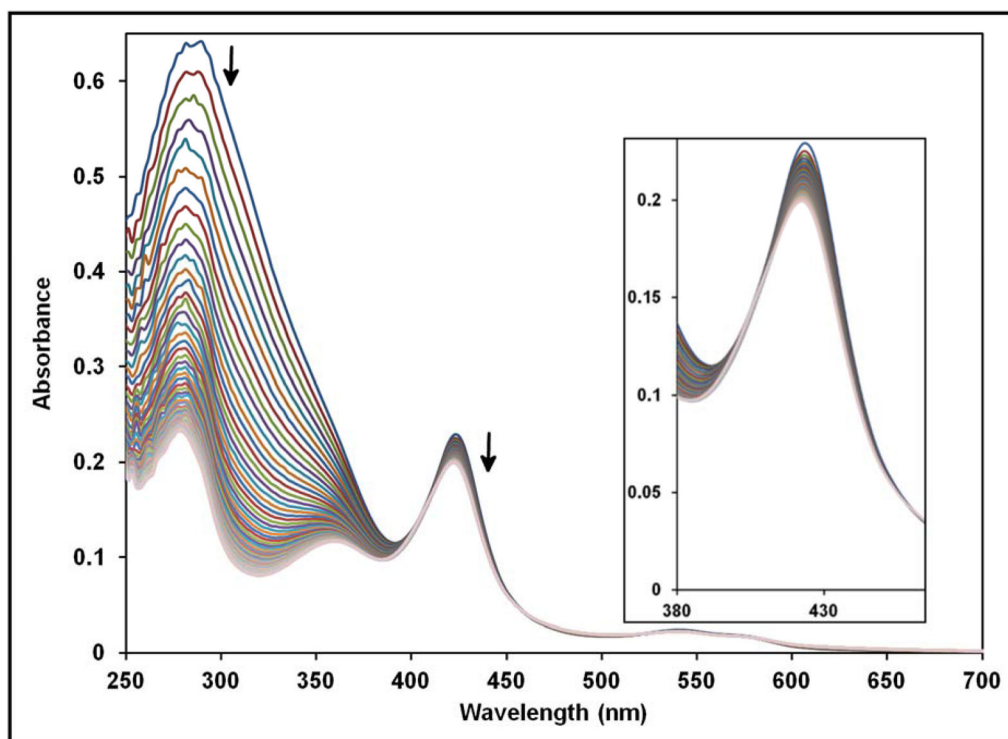


Figure 3. Diode Array spectrum of the reaction between 4 μM LmPP and 300 μM PN in 0.1 M potassium phosphate, pH 6.0. Arrows depict the direction of the absorbance change over time.

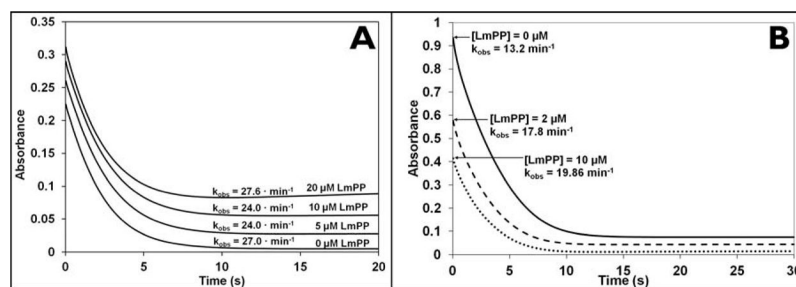


Figure 4. Rate constants for the decay of peroxynitrite mixed with various concentrations of LmPP, and measured at 302 nm by stopped-flow spectroscopy. (A) 250 μM peroxynitrite were mixed with 0, 10, 20, and 40 μM LmPP. (B) 1600 μM PN were mixed 0, 4, and 20 μM LmPP.

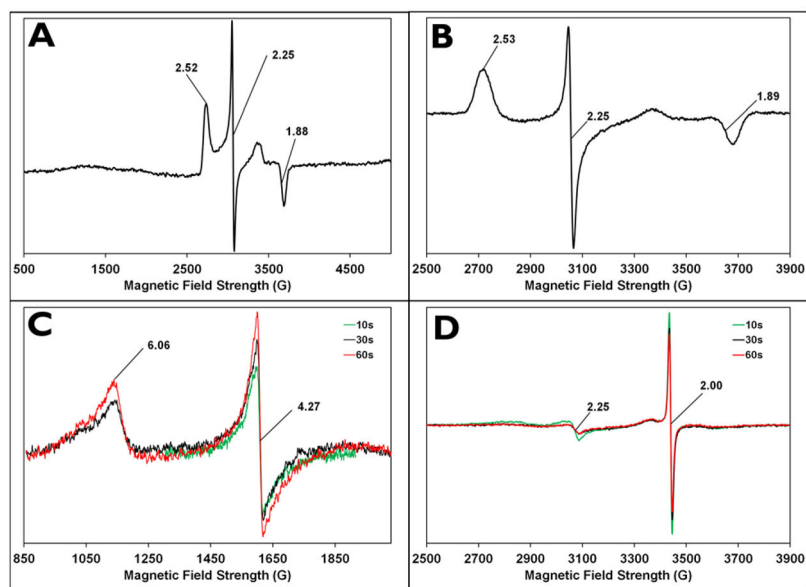


Figure 5. (A) Resting state X-band EPR spectrum of 0.1 mM LmPP in 0.1 M Tris, pH 9. (B) high field X-band EPR spectrum of 0.1 mM LmPP in 0.1 M Tris, pH 9. (C) Low field X-band EPR spectra of LmPP-PN timecourse samples. (D) High field X-band EPR spectra of LmPP-PN timecourse samples. All timecourse samples were freeze-quenched after 10s, 30s, and 60s.

Table 1

Crystallographic Data and Refinement Statistics.

Radiation source	SSRL BL 14-1
Space group	P 4 ₁ 2 ₁ 2
Unit cell dimensions a, b, c (Å)	63.68, 63.68, 152.49
Data resolution (Å) (highest-resolution shell)	48.88 (1.827 – 1.764)
X-ray wavelength (Å)	1.18076
Total no. of observations (highest shell)	573101 (51197)
No. of unique reflections (highest-resolution shell)	31236 (3100)
Completeness (%) (highest-resolution shell)	98.22 (94.03)
R_{merge} (highest-resolution shell)	0.7103 (3.476)
I/σ (highest-resolution shell)	73.11 (1.74)
CC_{1/2} (highest-resolution shell)	0.998 (0.297)
Redudancy (highest-resolution shell)	18.0 (16.5)
B factor, Wilson plot (Å²)	34.91
Number of protein atoms	2211
Number of heteroatoms	43
Number of waters	181
Disordered residues	49–55, 273–278, 340–341
R_{work}/R_{free}	0.1957/0.2184
Root-mean-squared deviation for bond lengths (Å)	0.007
Root-mean-squared deviation for bond angles (°)	1.05

Table 2

Observed rate constants for the decay of peroxyxynitrite as a function of pH measured by following the change in absorbance at 302 nm using stopped-flow spectroscopy.

pH	Rate constant, min ⁻¹	Temperature
9	0.498 ± 0.003	4 °C
9	1.39 ± 0.002	20 °C
7.5	13.2 ± 0.072	20 °C
4.36	88.1 ± 0.015	20 °C

Author Manuscript

Author Manuscript

Author Manuscript

Author Manuscript